Cell Reports

Active zone compaction correlates with presynaptic homeostatic potentiation

Graphical abstract

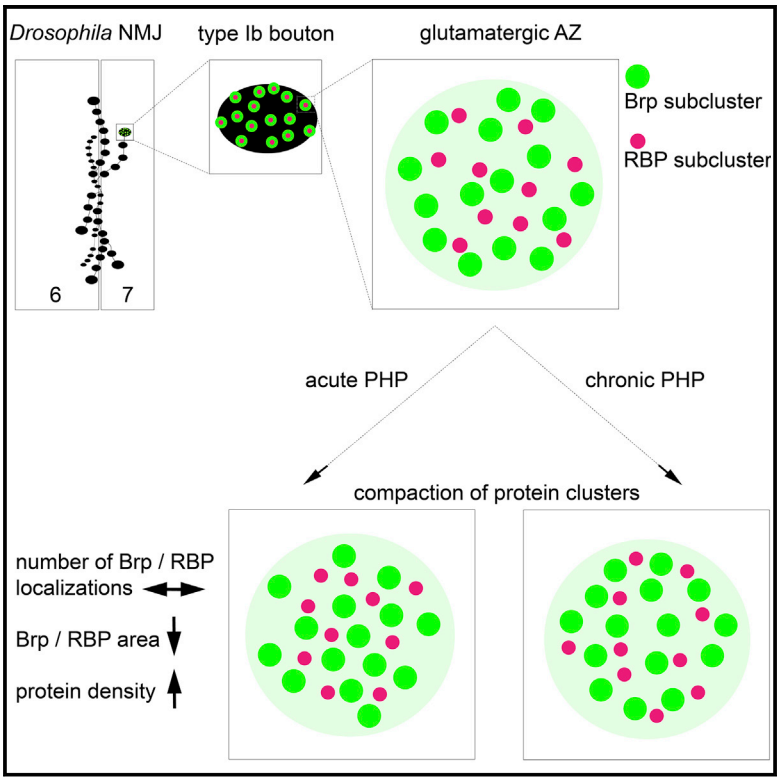

Highlights

- HDBSCAN analysis of dSTORM data allows precise determination of AZ nanotopology
- AZ compaction correlates with acute and chronic PHP
- AZ compaction comprises reduced AZ area and enhanced protein density
- Higher protein density equals apparent enlargement in confocal microscopy

Authors

Achmed Mrestani, Martin Pauli, Philip Kollmannsberger, ..., Anna-Leena Sirén, Manfred Heckmann, Mila M. Paul

Correspondence

heckmann@uni-wuerzburg.de (M.H.), mila.paul@uni-wuerzburg.de (M.M.P.)

In brief

Applying localization microscopy, Mrestani et al. introduce compaction of presynaptic active zone scaffolds and individual Bruchpilot and RIM-binding protein subclusters correlating with presynaptic homeostatic potentiation. Active zone compaction without protein recruitment enhances local molecule concentrations, which may be misjudged as enlargement by intensity-based imaging approaches.

Mrestani et al., 2021, Cell Reports *37*, 109770
October 5, 2021
https://doi.org/10.1016/j.celrep.2021.109770

Cell Reports

CellPress
OPEN ACCESS

Report

Active zone compaction correlates with presynaptic homeostatic potentiation

Achmed Mrestani,[1,8,9] Martin Pauli,[1,6,9] Philip Kollmannsberger,[2] Felix Repp,[1,2,6] Robert J. Kittel,[1,3,4] Jens Eilers,[4] Sören Doose,[5] Markus Sauer,[5] Anna-Leena Sirén,[1,6] Manfred Heckmann,[1,*] and Mila M. Paul[1,7,10,*]

[1]Institute for Physiology, Department of Neurophysiology, Julius Maximilians University Würzburg, 97070 Würzburg, Germany
[2]Center for Computational and Theoretical Biology, Julius Maximilians University Würzburg, 97074 Würzburg, Germany
[3]Institute of Biology, Department of Animal Physiology, Leipzig University, 04103 Leipzig, Germany
[4]Carl-Ludwig-Institute for Physiology, Leipzig University, 04103 Leipzig, Germany
[5]Department of Biotechnology and Biophysics, Julius Maximilians University Würzburg, 97074 Würzburg, Germany
[6]Department of Neurosurgery, University Hospital of Würzburg, 97080 Würzburg, Germany
[7]Department of Orthopaedic Trauma, Hand, Plastic and Reconstructive Surgery, University Hospital of Würzburg, 97080 Würzburg, Germany
[8]Department of Neurology, Leipzig University Medical Center, 04103 Leipzig, Germany
[9]These authors contributed equally
[10]Lead contact
*Correspondence: heckmann@uni-wuerzburg.de (M.H.), mila.paul@uni-wuerzburg.de (M.M.P.)
https://doi.org/10.1016/j.celrep.2021.109770

SUMMARY

Neurotransmitter release is stabilized by homeostatic plasticity. Presynaptic homeostatic potentiation (PHP) operates on timescales ranging from minute- to life-long adaptations and likely involves reorganization of presynaptic active zones (AZs). At *Drosophila melanogaster* neuromuscular junctions, earlier work ascribed AZ enlargement by incorporating more Bruchpilot (Brp) scaffold protein a role in PHP. We use localization microscopy (direct stochastic optical reconstruction microscopy [dSTORM]) and hierarchical density-based spatial clustering of applications with noise (HDBSCAN) to study AZ plasticity during PHP at the synaptic mesoscale. We find compaction of individual AZs in acute philanthotoxin-induced and chronic genetically induced PHP but unchanged copy numbers of AZ proteins. Compaction even occurs at the level of Brp subclusters, which move toward AZ centers, and in Rab3 interacting molecule (RIM)-binding protein (RBP) subclusters. Furthermore, correlative confocal and dSTORM imaging reveals how AZ compaction in PHP translates into apparent increases in AZ area and Brp protein content, as implied earlier.

INTRODUCTION

Chemical synapses are optimized for fast and reliable performance in combination with miniaturization and plasticity (Atwood and Karunanithi, 2002; Kittel and Heckmann, 2016; Neher and Brose, 2018). An intriguing form of plasticity is presynaptic homeostatic potentiation (PHP; Davis and Müller, 2015). PHP can be studied at *Drosophila* neuromuscular junctions (NMJs; Davis and Goodman, 1998; DiAntonio et al., 1999; Frank et al., 2006; Müller et al., 2012; Younger et al., 2013; Orr et al., 2017; Gratz et al., 2019). Although structural correlates of PHP remain elusive, several mechanisms are conceivable, including incorporation, removal and/or rearrangement of proteins at active zones (AZs), presynaptic membrane specializations where synaptic vesicles are discharged.

AZs are crowded mesoscale environments (Goodsell et al., 2020) with an organized set of proteins (Südhof 2012). Large α-helical coiled-coil proteins of the ELKS/CAST family are crucial for synaptic transmission (Held et al., 2016; Dong et al., 2018). In *Drosophila,* the ELKS/CAST homolog Bruchpilot (Brp) promotes synchronous glutamate release, and its amount correlates with release probability and synaptic differentiation (Kittel et al., 2006; Ehmann et al., 2014; Peled et al., 2014; Paul et al., 2015; Akbergenova et al., 2018). Brp is a major scaffold for fast transmitter release (Kittel et al., 2006; Held and Kaeser, 2018). Whereas its N terminus (N term) has been mapped in membrane proximity, its C-terminus (C term) localizes ~155 nm above postsynaptic receptors (Fouquet et al., 2009; Liu et al., 2011) and is important for tethering synaptic vesicles (Hallermann et al., 2010). Remarkably, Brp is distributed heterogeneously, forming about 15 subclusters (SCs) within an AZ (Ehmann et al., 2014). SCs with high protein concentration should promote vesicle tethering (Sieber et al., 2007; Barg et al., 2010; van den Bogaart et al., 2011). Early work has shown no evidence of protein synthesis during PHP (Frank et al., 2006), but imaging has suggested an increased Brp amount during PHP (Weyhersmüller et al., 2011; Goel et al., 2017, 2019; Böhme et al., 2019; Hong et al., 2020).

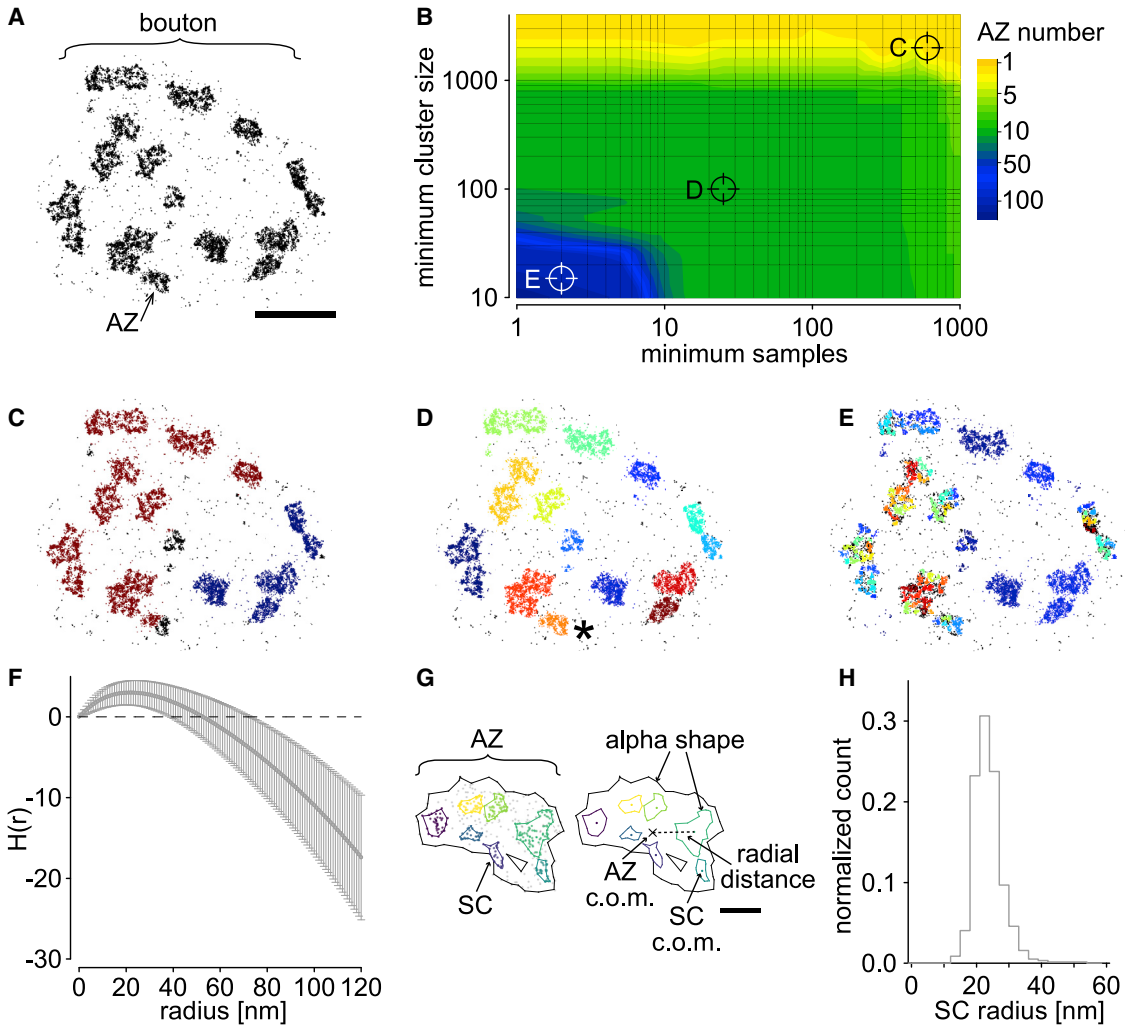

Figure 1. Cluster analysis of presynaptic Brp localizations

(A) Scatterplot of dSTORM localizations of a wild-type (WT) Ib bouton stained for Brp^{Nc82}. An arrow indicates an individual Brp cluster or AZ.

(B) Contour plot of the number of detected AZs in the data from (A) depending on the HDBSCAN parameters minimum samples and minimum cluster size.

(C–E) Data from (A) after HDBSCAN. Colors indicate clusters, with unclustered localizations in black. Minimum cluster size and minimum samples were 2,000 and 600 (C), 100 and 25 (D), and 15 and 2 (E). AZs are merged into two large clusters in (C) and split in (E). An asterisk highlights a cluster in (D) shown in (G).

(F) Averaged H function (gray, mean ± SD) from 568 AZs from 13 NMJs of 6 WT animals. The maximum of the curve indicates a mean subcluster (SC) radius of 22 nm. A dashed line indicates prediction for a random Poisson distribution.

(G) HDBSCAN for SC detection applied to an AZ. Black lines indicate alpha shapes used for AZ area quantification. Left: a colored Brp SC surrounded by colored lines indicating alpha shapes. Gray dots represent unclustered localizations. Right: centers of mass (c.o.m.) of the AZ (cross) and of SCs (colored dots) are indicated. A dashed line shows the Euclidean distance between the AZ c.o.m. and an SC c.o.m., referred to as radial distance.

(H) Histogram of mean Brp SC radius per AZ assuming a circular area; median (25th–75th percentile), 23 (21–26) nm) for AZs in (F).

Scale bars, 1 μm (A) and 100 nm (G).

Here we reason that localization microscopy in terms of *direct* stochastic optical reconstruction microscopy (dSTORM; Heilemann et al., 2008; van de Linde et al., 2011) permits precise quantification of Brp and Rab3 interacting molecule (RIM)-binding protein (RBP; Ehmann et al., 2014; Paul et al., 2015). For unbiased data analysis, we perform hierarchical density-based spatial clustering of applications with noise (HDBSCAN; Campello et al., 2013) and address the following questions. How robust are dSTORM results? Does the protein amount within AZs increase during PHP, and/or do AZs grow or shrink?

RESULTS

Analysis of super-resolution data

We imaged type Ib boutons using dSTORM (Figure 1A; Heilemann et al., 2008; van de Linde et al., 2011; Löschberger et al., 2012; Ehmann et al., 2014; Paul et al., 2015) and a highly specific monoclonal antibody, Brp^{Nc82}, that maps to the C-terminal region of Brp (Kittel et al., 2006; Fouquet et al., 2009). Because Brp is an abundant protein and the epitope covers the spatial extent of an AZ, we interpret "Brp area" as "AZ

area." We used a Python implementation of HDBSCAN, extracting clusters in data with varying density (Campello et al., 2013; McInnes et al., 2017). To test the algorithm, we varied its free parameters minimum cluster size and minimum samples and analyzed their influence on cluster number, localizations, and area per cluster (Figures 1B–1E; Figure S1). A wide range of parameters delivered robust results, and all Brp clusters in the following were extracted with the combination 100 and 25 for minimum cluster size and minimum samples, respectively.

To probe the existence of Brp SCs in our data, we computed H functions (derivative of Ripley's K function) and calculated an averaged curve (Figure 1F). Positive values for H(r) indicate clustering, negative dispersion or edge effects, and maximum positive values roughly correspond to the radius of putative clusters (Kiskowski et al., 2009). The curve maximum at 22 nm agrees with the dimensions of SCs reported earlier (Ehmann et al., 2014). Subsequently, we performed a second HDBSCAN on Brp clusters with adjusted parameters that yielded similar SC radii as the H function (Figures 1G and 1H). In addition to alpha shape generation for area determination, a center of mass (c.o.m.) of the entire cluster and of all SCs and their specific interspaces was measured (Figure 1G). The distance between AZ c.o.m. and SC c.o.m. is referred to as radial distance.

Compaction of the Brp scaffold in acute and chronic PHP

Philanthotoxin (PhTx) induces PHP and increases quantal content (Frank et al., 2006; Weyhersmüller et al., 2011; Davis and Müller, 2015). We compared AZs incubated in PhTx (phtx) or DMSO (control; Figure 2A). Brp localization numbers as a measure of protein amount per AZ (Ehmann et al., 2014) were not changed in phtx, but Brp cluster area was reduced compared with controls; hence, Brp density increased in phtx (Figure 2B; Table S1A). Thus, PHP induces a rearrangement of Brp without changing protein numbers within AZs. Previous work discovered a gradient with distal Ib boutons containing more AZs and more Brp and releasing more glutamate than proximal ones (Peled and Isacoff, 2011; Ehmann et al., 2014; Paul et al., 2015). To test whether the changes in phtx described above occur in a spatial pattern, we performed a subgroup analysis of AZs in boutons 1–6 (Paul et al., 2015). Spearman correlation displayed no correlation between bouton number and Brp localization density in both groups (Figure S2A). Thus, structural plasticity in acute PHP occurs homogeneously within NMJs. Furthermore, there was no change in the total number of localizations or in the amount of unclustered localizations outside of AZs per bouton (Figure S2B). Next we quantified the circularity of Brp clusters as the ratio of their eigenvalues of the covariance matrix (ratio between 0 and 1, with 1 indicating a perfect circle; i.e., presumably in top view). Cluster circularity was similar in phtx and control; thus, analysis of the entire data without selection appeared to be appropriate. Interestingly, analyzing the relation between AZ area and circularity uncovered an inverse correlation (Figure S2C). We interpret this as low circularity being indicative of AZs in side view or of large spots partially arising from merged AZs lying nearby in 2D projection. The latter have been referred to as double ring structures, grouped units, or cluster AZs (Kittel et al., 2006; Ehmann et al., 2014; Akbergenova et al., 2018). Assuming that some parameters depend on orientation, we analyzed area and radial distance in a subsample with a circularity of 0.5 or greater; i.e., planar orientation (Figure S2D). We found a pronounced decrease in area and a similar decrease in radial distance, indicating that Brp compaction appears regardless of AZ orientation.

To test whether compaction is a general phenomenon in PHP, we used knockout of the postsynaptic glutamate receptor subunit GluRIIA as a chronic PHP model (GluRIIAKO; Petersen et al., 1997; DiAntonio et al., 1999; Frank et al., 2006). We performed dSTORM in GluRIIAKO and the wild type (WT) as described (Figure 2C). Remarkably, we found comparable effects with unchanged Brp localization numbers per AZ, decreased AZ area, and higher Brp density (Figure 2D). Thus, Brp scaffolds are also compacted in chronic PHP.

Previous work has shown that chronic PHP only occurs at type Ib but not Is boutons (Newman et al., 2017). In contrast, Genç and Davis (2019) postulated that chronic and acute PHP can be expressed in both bouton types but strongly depend on extracellular calcium. We compared Brp clusters of type Ib and Is boutons (Figures S2E and S2F). Type Is clusters contain less localizations within a smaller area and, therefore, exhibit a higher protein density; i.e., they are compacted. We also probed Brp cluster organization in type Is boutons after PhTx treatment (Figure S2G) and found no further compaction in a calcium-free environment.

AZ SC compaction

We tested whether Brp reorganization during PHP also takes place at the level of Brp SCs (Figures 2E and 2G). SC number per AZ was unchanged in phtx and GluRIIAKO (Figures 2F and 2H). Although Brp localization numbers in SCs were unchanged, SC area was decreased (Figures 2F and 2H). Thus, mean Brp localization density in SCs is increased in PHP. We also examined radial distances between the c.o.m. of an individual AZ and SC c.o.m. and found them to be decreased (Figures 2F and 2H). In addition, the minimum distance between SC c.o.m. was decreased in PHP, whereas the space between SCs was only reduced in chronic PHP (Figures S2H–S2K). These data show compaction within SCs in acute and chronic PHP, but the number of Brp molecules is not increased. Because PhTx effects were imaged at muscle 4 (Goel et al., 2017; Böhme et al., 2019), we also imaged phtx AZs on muscle 4 and applied our analysis with similar results (Figure S3).

Correlative confocal-dSTORM imaging of AZs

Earlier imaging has reported increased fluorescence intensity in PHP and interpreted this as evidence of protein recruitment to AZs (Weyhersmüller et al., 2011; Goel et al., 2017; Böhme et al., 2019). Because our results are in sharp contrast, we wondered whether the difference in molecular density before and after PHP could bias Brp area quantification in our localization-based or in intensity-based approaches. To test this, we compared both methods using simulated circular clusters without noise and subclustering (Figure S4). Our results indicate that the area of large objects with low molecular density (i.e., lower fluorescence intensity) can be grossly misjudged by pixel- and intensity-based quantification, which could explain the mentioned discrepancy. Next we performed sequential confocal

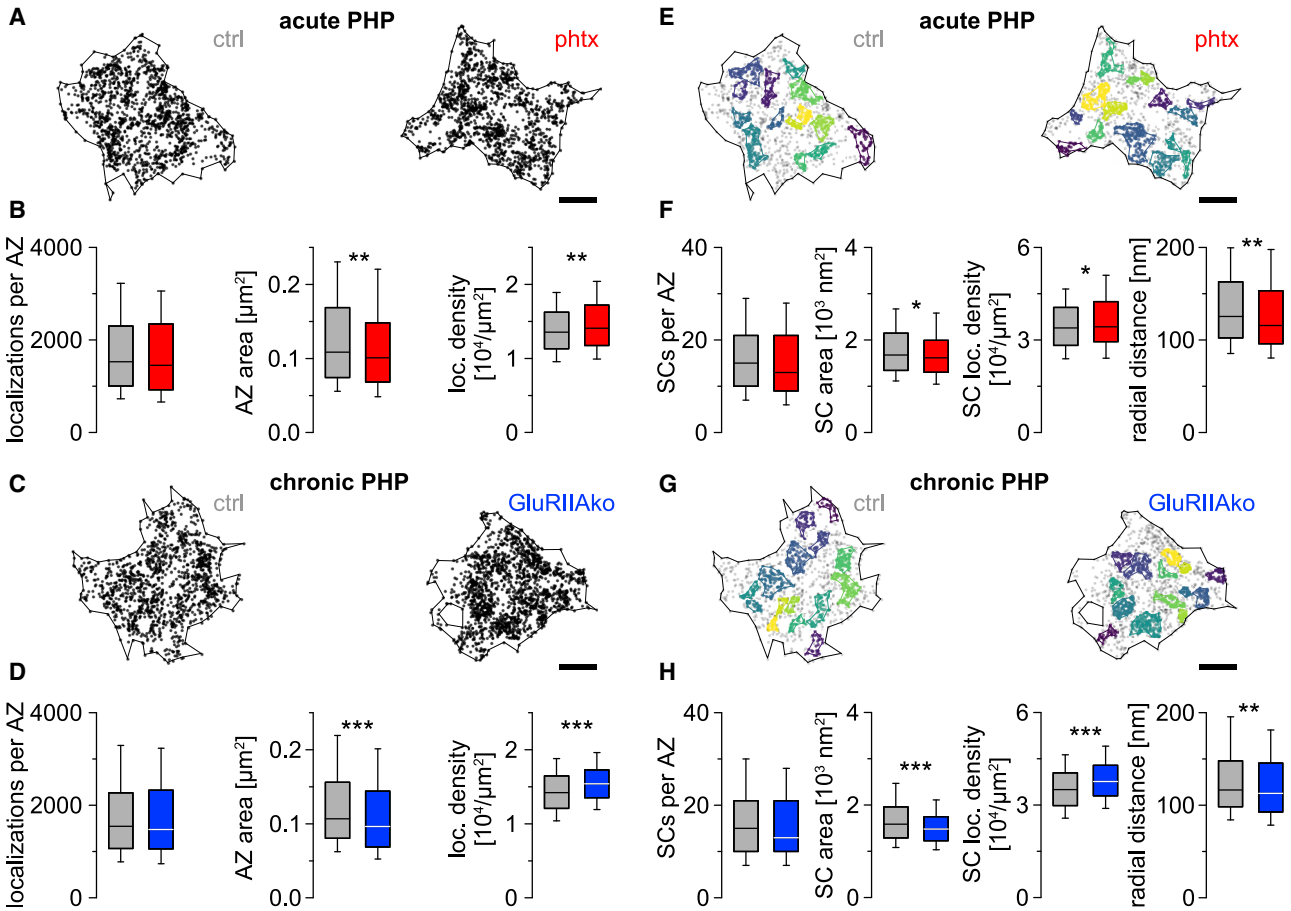

Figure 2. Acute and chronic PHP decrease AZ area and increase Brp density in clusters and SCs

(A) Scatterplots of Ib AZs from a control (ctrl) and a philanthotoxin-treated animal (phtx).

(B) Number of Brp localizations per AZ ($p = 0.236$), AZ area ($p = 0.009$), and Brp localization density ($p = 0.009$) for ctrl (gray, n = 568 AZs from 13 NMJs of 6 animals) and phtx larvae (red, n = 792 AZs from 14 NMJs of 5 animals), shown as boxplots, where horizontal lines represent median, boxes quartiles, and whiskers 10th and 90th percentiles. Asterisks indicate significance level (*$p < 0.05$, **$p < 0.01$, ***$p < 0.001$).

(C) Scatterplots of type Ib AZs from a ctrl animal and a GluRIIA receptor null mutant (GluRIIAKO).

(D) Number of Brp localizations per AZ ($p = 0.391$), AZ area ($p < 0.001$), and Brp localization density ($p < 0.001$) for ctrl (gray, n = 872 AZs from 19 NMJs of 6 animals) and GluRIIAKO (blue, n = 1,020 AZs from 19 NMJs of 6 animals).

(E) Scatterplots of Ib AZs from ctrl and phtx. Brp SCs are colored, and unclustered localizations are displayed as gray dots. Localizations outside of the alpha shape are not shown for clarity.

(F) Number of SCs per AZ ($p = 0.084$), SC area ($p = 0.025$), SC localization density ($p = 0.022$), and radial distance between the AZ c.o.m. and SC c.o.m. ($p = 0.003$) for ctrl (gray, n = 568 AZs from 13 NMJs of 6 animals) and phtx (red, n = 792 AZs from 14 NMJs of 5 animals).

(G) Scatterplots of Ib AZs from ctrl and GluRIIAKO as shown in (E).

(H) Number of SCs per AZ ($p = 0.118$), SC area ($p < 0.001$), SC localization density ($p < 0.001$), and radial distance ($p = 0.002$) for ctrl (gray, n = 872 AZs from 19 NMJs from 6 animals) and GluRIIAKO (blue, n = 1,020 AZs from 19 NMJs of 6 animals).

Scale bars, 100 nm (A, C, E, and G).

dSTORM imaging of Brp (Figures 3A and 3B). Confocal data were analyzed with an intensity threshold of 100 a.u. (Figure 3Aii). Figure 3C shows Brp overlaid in confocal microscopy and dSTORM and demonstrates area overestimation because of high localization density (Figure 3Ci) and that thresholding of confocal data can lead to complete loss of signal included in dSTORM (Figure 3Cii). Additionally, segmentation of closely spaced clusters is clearly superior using HDBSCAN of localization data compared with thresholding-based quantification of confocal data (Figure 3Ciii). We quantified AZs in the complete dataset. AZ area distribution was broader in confocal microscopy than in dSTORM (Figure 3D). As expected, we obtained positive correlations between localization density per AZ and mean pixel intensity per AZ (Figure 3E). Interestingly, localization density correlated stronger with confocal microscopy- than dSTORM-measured AZ area (Figure 3F), matching simulations (Figure S4). Confocal microscopy mostly overestimates cluster area, whereas underestimation occurs at low localization density (Figure 3G). This indicates that higher density in dSTORM leads to an apparent area enlargement in thresholded confocal imaging.

CellPress
OPEN ACCESS

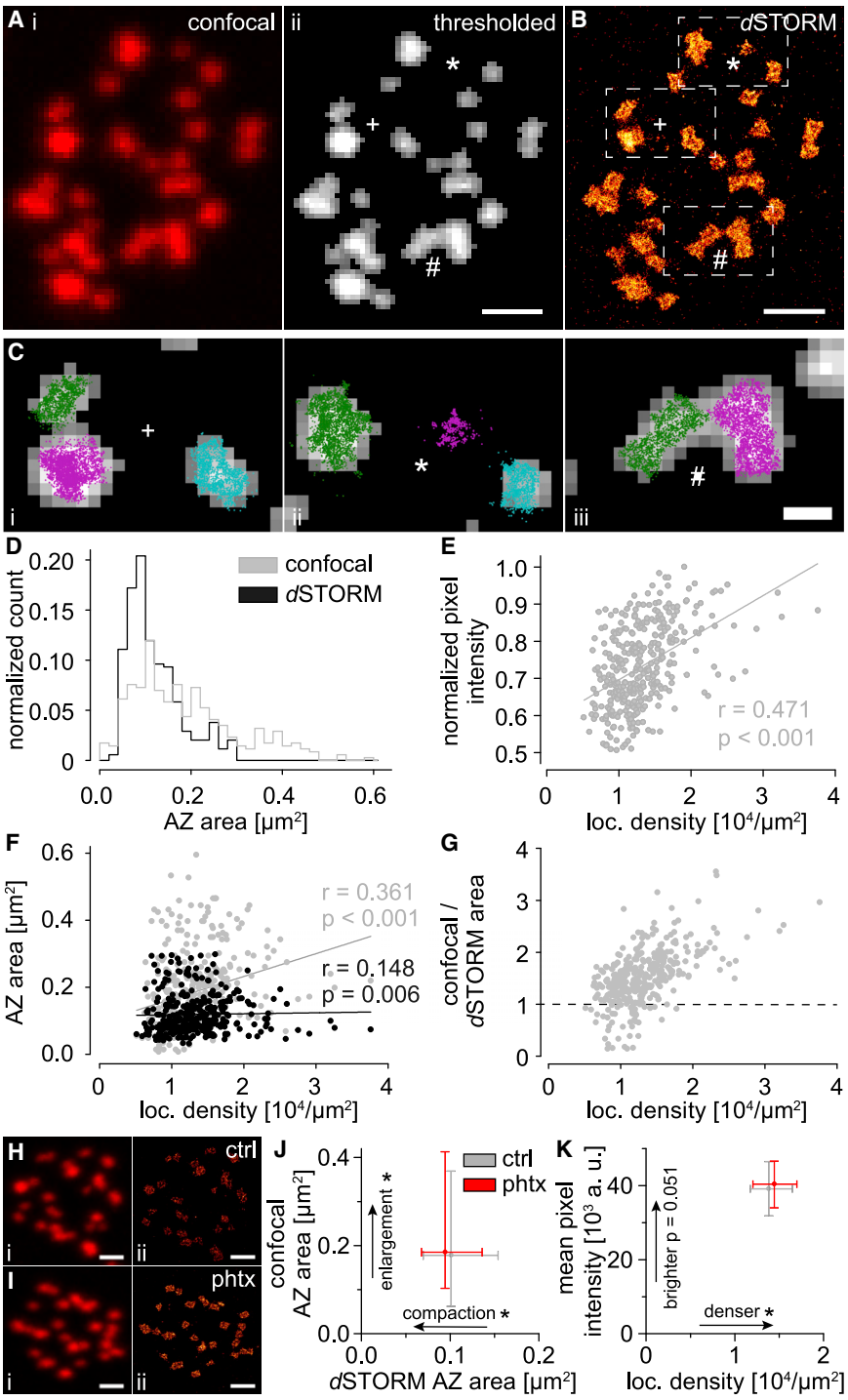

Figure 3. Correlative confocal-dSTORM links increased localization density to increased confocal intensity and Brp area

(A) Confocal image of a type Ib bouton. (i) Unprocessed original image. (ii) After applying a 100 a.u. threshold. Symbols mark corresponding regions in (B).

(B) dSTORM image of the bouton in (A). Boxes correspond to enlarged regions in (C).

(C) Enlarged confocal AZs (gray) and overlaid scatterplots of Brp dSTORM localizations (green, magenta, and blue). Localizations at the edges are not displayed. The green and magenta clusters in (i) are not separated in confocal microscopy, the magenta cluster in (ii) is lost after confocal thresholding, and clusters in (iii) are not separated.

(D) AZ area measured with confocal microscopy (gray) and dSTORM (black).

(E and F) Spearman correlation coefficient of normalized mean confocal pixel intensity and dSTORM localization density (E) as well as AZ area in confocal imaging and localization density (F, gray) compared with AZ area in dSTORM and localization density (black).

(D–F) n = 343 AZs from 12 NMJs of 7 animals.

(G) Ratio of confocal microscopy and dSTORM areas of AZs plotted against localization density. Values below 1 (dashed line) indicate underestimation in confocal quantification with respect to *d*STORM, whereas values above 1 indicate overestimation.

(H and I) Confocal images of a ctrl (H, i) and phtx Ib bouton (I, i) and the same boutons imaged with dSTORM (H, ii, and I, ii).

(J) AZ area in confocal (median [25th–75th percentile]) plotted against AZ area from dSTORM analysis in ctrl (gray, n = 399 confocal AZs and 477 *d*STORM AZs from 14 NMJs of 7 animals) and phtx (red, n = 481 confocal AZs and 647 *d*STORM AZs from 15 NMJs of 7 animals, p = 0.025 and 0.027 for the x and y axis, respectively).

(K) Mean pixel intensity in confocal data plotted against dSTORM localization density in ctrl and phtx (p = 0.011 and 0.051 for the x and y axis, respectively).

(J and K) Asterisks denote significant differences reported by confocal and dSTORM analyses.

Scale bars, 1 µm (A, B, H, and I) and 330 nm (C).

Homeostatic compaction is translated into an apparent area increase

In contrast to earlier work (Weyhersmüller et al., 2011; Goel et al., 2017; Böhme et al., 2019) we found smaller Brp areas but increased localization density in PHP. To address this discrepancy, we applied a Gaussian filter of 150 nm SD to our data to obtain confocal resolution (Figures S5A and S5B). 3D histograms of example AZs illustrate the thresholding (Figure S5C; compare Figure 4B in Weyhersmüller et al., 2011). In phtx, AZ area is decreased and localization density increased in dSTORM (x axes, Figures S5D and S5E), whereas AZ area and mean pixel intensity are increased in the same images in Gaussian-filtered data (y axes). We conclude that intensity-based quantification with confocal resolution may lead to inverse results for Brp area compared with localization-based analysis. Next we applied a Gaussian filter of 25 nm SD to our data to obtain STED (stimulated emission depletion) resolution (Figure S5F).

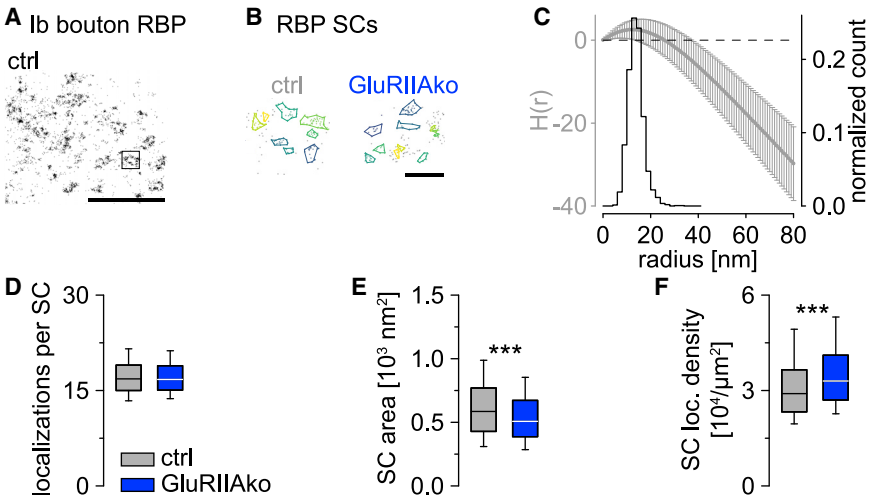

Figure 4. Compaction of RBP SCs at GluRIIAKO AZs

(A) Scatterplot of dSTORM localizations of a ctrl Ib bouton stained against RBP.

(B) RBP SCs extracted by HDBSCAN in ctrl (enlarged from A) and GluRIIAKO. For a detailed description, see Figure 2E.

(C) Averaged H function from 1,450 RBP clusters from 18 NMJs of 6 WT animals (maximum of the curve indicates a mean SC radius of 12 nm) and histogram of mean SC radius (estimated from mean SC area per cluster, assuming a circular area, median [25th–75th percentile]: 13.7 (11.7–15.7) nm) for the same clusters.

(D–F) Number of localizations per SC (D, $p = 0.992$), SC area (E, $p < 0.001$), and SC localization density (F, $p < 0.001$) for ctrl (gray, n = 1,450 RBP clusters from 18 NMJs of 6 animals) and GluRIIAKO (blue, n = 1,245 RBP clusters from 16 NMJs of 6 animals).

Scale bars, 1 µm (A) and 100 nm (B).

AZ diameter was estimated from AZ area, and intensity maxima per AZ were detected in selected planar-oriented AZs with a peak finding algorithm in FIJI after thresholding (Böhme et al., 2019). This indicated an increase in AZ area, diameter, and number of intensity maxima per AZ after PHP induction (Figure S5G), findings apparently contrary to localization-based analysis. The larger AZ diameter in our "STED analysis" compared with earlier work (Kittel et al., 2006; Weyhersmüller et al., 2011) arises from distinct quantification because we used the whole AZ area to calculate the diameter under the assumption of a circular area, whereas earlier studies used peak-to-peak distances in intensity profiles of ring-like Brp structures. Gaussian filtering of dSTORM data gives inverse results for the number of clusters per AZ, matching the aforementioned findings. To further probe this, we performed sequential confocal-dSTORM in control (ctrl) and phtx (Figures 3H and 3I). Correlative imaging delivered the same results as the Gaussian filtering regarding AZ area, localization density, and mean pixel intensity (Figures 3J and 3K). Interestingly, the changes reported by confocal microscopy critically depend on the intensity threshold used for quantification (Figures S5H and S5I).

RBP SC compaction at GluRIIAKO AZs

To probe whether compaction also occurs within clusters of AZ proteins close to the membrane, we performed dSTORM and a two-level HDBSCAN of RBP at GluRIIAKO and WT NMJs (Figure 4). Because of a lower signal-to-noise ratio and overall fewer localizations per cluster compared with Brp, the algorithm did not allow robust identification of RBP clusters. However, it provided robust results for RBP SC organization (Figures 4A and 4B). To measure the spatial extent of these SCs, we again computed H functions (Figure 4C). We found the maximum of the curve at 12 nm, substantially smaller than for Brp SCs, and adjusted HDBSCAN parameters to yield similar results for SC radii as the H function. RBP SCs in GluRIIAKO are significantly smaller than in the WT with unchanged localization numbers (Figures 4D and 4E). Accordingly, RBP localization density increased (Figure 4F). These data reveal that compaction also occurs in PHP in membrane proximity and, therefore, may be a general phenomenon.

Compaction of the AZ mesoscale in 3D

The analysis so far was based on the assumption that AZs from different NMJs within the same group are drawn from the same distribution. However, further variance analysis showed considerable differences between NMJs of the same treatment group (Table S1B). Thus, we performed statistical analyses of the parameter localizations per AZ, AZ area, and localization density, considering values for pooled images as statistical reference as opposed to individual AZs, as shown so far (Figure S6; Table S1C). Unchanged localizations per AZ and reduced AZ area could be confirmed, but significance for the increase in density was only reached for chronic PHP. However, this approach is underpowered and likely underestimates the effects (Table S1C). We computed a linear mixed model on our data, treating PHP as a fixed effect and the differences between NMJs as a random effect (Figure S7; Table S1D). This approach accounts for inter-NMJ variability while avoiding pooling by using all data points for fitting. Confidence intervals of the model coefficients were determined by bootstrapping of resampled data (10,000 repetitions; DiCiccio and Efron, 1996) and p values were derived from the confidence intervals of the estimate, as described previously (Altman and Bland, 2011). All model fits converged, and residuals were distributed normally and independent of the predicted variable (Figures S7A–S7F). This supports the conclusion that the structural effects in PHP are not due to random sample variability (Figures S7G–S7I). Furthermore, we performed simulations of 2D super-resolution data distributed within a 3D hemisphere resembling a Brp SC (Figure 5A). We included the linkage error, which displaces molecule coordinates by a fixed amount in a random direction (Figure 5B). This displacement is important because it increases the size of the original to a substantially larger localization radius. Thus, the simulation shows that a moderate change in 2D localizations translates into a larger change in 3D molecule concentration, which is the physiologically relevant parameter (Figures 5C and 5D). Changing the

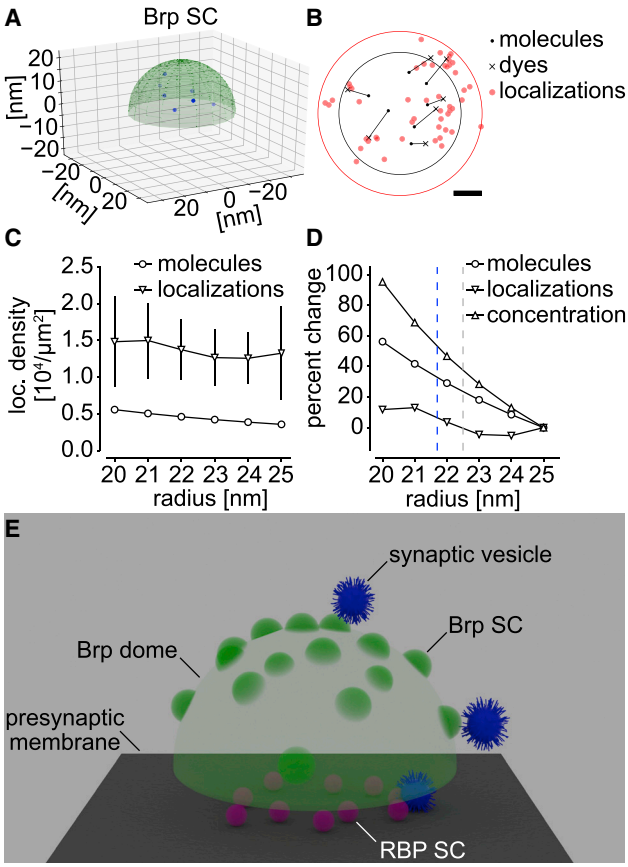

Figure 5. Molecular compaction in a 3D hemisphere

(A) Simulations of 2D dSTORM data, illustrating how changes in measured 2D molecule density correspond to changes in 3D molecule concentration. 7 Brp molecules (blue dots) are distributed uniformly within a hemisphere of 22 nm radius as measured for Brp SCs (green dome).

(B) 2D projection of the molecules shown in (A) (black dots) and illustration of original coordinate displacement. A red circle shows the increase in effective radius (black circle) because of linkage error (13 nm) and localization precision (7 nm). 7 localizations per molecule are shown (red dots). Scale bar, 10 nm.

(C) Summary graph of projected 2D density of Brp molecules (circles) and measured 2D localizations (triangles) for fixed radii between 20 and 25 nm.

(D) Summary graph of the percent change of the Brp localization density for 2D localizations (tip-down triangles), 2D projected molecule density (circles), and 3D concentration (tip-up triangles) relative to a radius of 25 nm (C). Dotted lines indicate Brp SC radii in ctrl (gray, 22.5 nm) and GluRIIAKO (blue, 21.7 nm).

(C and D) n = 50 simulated clusters per radius.

(E) 3D model of a ctrl *Drosophila* AZ generated in Blender. Synaptic vesicles (blue, diameter of 40 nm, protein coat of 10 nm) are shown on the surface of a Brp dome (green), which has a diameter of 370 nm and bears 15 smaller domes on its surface, representing SCs (each resembling a 3D hemisphere shown in A) with diameters of 45 nm arranged in ~116 nm radial distance. When viewed from above, the SC arrangement will appear donut- or ring-like (Kittel et al., 2006) because the epitopes spaced uniformly across the 3D dome are collapsed into two dimensions. Below the dome, 10 RBP SC spheres (magenta) are arranged in membrane proximity within a radial distance of ~97 nm. Vesicles are tethered to the Brp dome and docked to release sites at the membrane.

SC radius from 25 nm to 20 nm results in an increase in projected 2D Brp density (Figure 5C, circles); although the measured density is higher, it changes only slightly with decreasing radius. The difference is visible when plotted as percent change relative to a baseline radius of 25 nm (Figure 5D); although the measured density is less than 20% higher at 20 nm compared with 25 nm, the projected 2D density is 60% higher, and the physiologically relevant 3D density is almost 100% higher, because 3D density scales with the cube of the radius. This supports the hypothesis that small but robust changes in 2D dSTORM might have important functional implications in a 3D hemisphere, but the mechanistic interpretations are still unknown. In addition, we generated a 3D model of an AZ derived from our quantitative data (Figure 5E; Figure S8; Video S1). This model illustrates how AZs are compacted during PHP.

DISCUSSION

We introduce AZ compaction as a mechanism for presynaptic structural adaptation in acute and chronic PHP. It encompasses a reduced AZ area and enhanced molecular density without increasing protein counts. This holds true for the membrane-distant Brp^{Nc82} epitope organized in clusters and SCs, which are likewise compacted and located closer to AZ centers. RBP SCs are also compacted. Notably, compaction of Brp and RBP appears as an increase in AZ area in thresholding-based analysis, explaining the apparent contradiction with earlier results.

The 3D mesoscale of the AZ

We reason that dSTORM and HDBSCAN is a powerful combination to decipher protein dense networks. The reported effects are small in absolute terms but reproducible under different conditions (Figures 2, 3, and 4; Figures S2 and S3). Brp analysis shows a higher protein density in phasic Is terminals compared with tonic Ib. The higher release probability at type Is AZs (Lu et al., 2016; Newman et al., 2017; Aponte-Santiago and Littleton, 2020) correlates to the compacted Brp scaffold and is iterated in acute and chronic PHP in type Ib boutons. Previous work has postulated that chronic PHP only takes place in type Ib boutons (Newman et al., 2017), but more recent work controversially stated that acute and chronic PHP can be expressed at both bouton types (Genç and Davis, 2019). However, expression depends on extracellular calcium. In light of mechanistic considerations, it is plausible that changes in molecular proximities in the nanometer range lead to considerable functional consequences (Neher 1998). For example, it is established for Syntaxin that clusters enhance local protein concentration, which, in turn, may raise the probability of protein interactions (Sieber et al., 2007; Barg et al., 2010; van den Bogaart et al., 2011). Furthermore, in hippocampal neurons, RIM clusters with diameters of ~80 nm show reorganization during plasticity (Tang et al., 2016). Concentrations can be estimated from our data and Brp protein numbers per AZ reported by Ehmann et al. (2014), assuming a distribution of the Brp^{Nc82} epitope in a hemisphere. For radii of 185 and 175 nm (Figure 2D; Table S1), hemisphere volumes before and after PHP are ~0.013 and 0.011 µm^3, respectively. 170 Brp molecules (Ehmann et al., 2014) yield concentrations of 21 and 25 µM before and after PHP, respectively. Thus, the ~7% density increase translates into a 19% concentration increase (Figures 5A–5D). Brp SCs are assumed to

contain bundles of ~7 Brp proteins (Ehmann et al., 2014), creating a platform for a synaptic vesicle. For hemispheres with SC radii of 22.5 and 21.7 nm (Figure 2H), this yields Brp concentrations of 490 and 540 μM before and after PHP, respectively. Although the abovementioned estimates for Brp clusters are probably reasonably accurate, the estimates for the concentration in SCs provide only a lower limit. Here, SC radii are most certainly overestimated because of the linkage error introduced by the combination of a primary antibody with the secondary $F(ab')_2$ fragment, leading to a labeling complex diameter of 26 nm (Ehmann et al., 2014). Thus, local protein concentrations could be even higher and, likewise, the difference in the two scenarios. This could be clarified by using smaller labeling approaches; e.g., directly fluorophore-conjugated Brp^{Nc82} $F(ab')_2$ fragments. Brp has been shown to tether synaptic vesicles via its C term (Hallermann et al., 2010; Scholz et al., 2019). Vesicle traffic with Brp C terms in liquid-liquid phase separation (Milovanovic et al., 2018) could profit from AZ compaction. Although the molecular binding partners of the Brp C term are still unclear, a functional interaction with Complexin has been reported (Scholz et al., 2019). Other coiled-coil proteins, like Golgins, tether and traffic vesicles at the Golgi network by guidance via multiple vesicle-binding sites (Gillingham and Munro, 2016; Cheung and Pfeffer, 2016). Likewise, Brp could provide a meshwork guiding vesicles via multiple interaction sites represented by SCs. HDAC6-dependent deacetylation of its C term essentially regulates Brp function, emphasizing the importance of vesicle tethering and transmitter release (Miskiewicz et al., 2014). Taking the ~40.5-nm vesicle diameter from Karunanithi et al. (2002) and adding ~10 nm of protein trimmings (Takamori et al., 2006) results in 50- to 60-nm veritable vesicle extent. This corresponds to the reduced Brp SC center distance during PHP, perhaps favoring vesicle traffic over the surface (Figure 5E; Video S1). In our 3D model, Brp SCs are shown as small domes that, because of their round structure, have a minimal surface and, thus, larger inter SC distances compared with the real data (Figures S2J and S2K). Furthermore, in our model, SCs are static, whereas it is reasonable to assume that *in vivo* SCs are dynamic, which should further facilitate vesicle movement on the surface of the dome. These structural adaptations may be in line with an increased number of release-ready vesicles; i.e., increased RRP (readily releasable pool) size during PHP (Weyhersmüller et al., 2011; Delvendahl et al., 2019). Assuming that all Brp molecules forming one SC create a platform for vesicle tethering matches reasonably well with electron microscopy (EM) studies describing, on average, 12 vesicles tethered to a single CAZ (Böhme et al., 2016) and with reconstructions of EM tomography data (Zhan et al., 2016).

Compaction of the AZ scaffold without protein recruitment

The number of Brp localizations did not change during PHP, in line with previous work ruling out protein synthesis during PHP (Frank et al., 2006). Confocal and STED data have been interpreted as evidence of protein incorporation into AZs (Weyhersmüller et al., 2011; Goel et al., 2019), even when the axon is cut from the soma (Goel et al., 2017) or in the presence of translation inhibitors (Böhme et al., 2019). Structured illumination microscopy suggested that PhTx treatment increases individual Brp spots and promotes formation of AZs with multiple Brp rings (Hong et al., 2020). In accordance, STED imaging discovered increasing ring diameters (Weyhersmüller et al., 2011) and increasing numbers of AZ nano-modules during PHP (Böhme et al., 2019; Goel et al., 2019). However, our data support an alternative interpretation (Figures 2B and 2D; Figure S2B). Our imaging shows that Brp SCs are arranged uniformly within an individual AZ. We interpret this arrangement on the surface of a hemisphere-like structure (Figure 5E) appearing as a donut- or ring-like organization in lower-resolution imaging (Kittel et al., 2006). However, this occurs only in AZs viewed from above as a result of axial image projection (Video S1). We show that large structures with low intensity appear smaller than small structures with higher intensity (Figure S4C) and that higher protein density in dSTORM translates into an apparent area increase in confocal microscopy (Figure 3F). In confocal microscopy, usually a stack of multiple slices is obtained, whereas 2D dSTORM only samples signal from a single focal plane. However, we found no evidence of signal in confocal microscopy missing in corresponding dSTORM images (Figures 3Ai and 3B). We measured a z-range of boutons in confocal stacks ranging from 800 nm to 2 μm, roughly corresponding to the axial capture range of dSTORM (Tokunaga et al., 2008). The correlation between localization density and AZ area in confocal microscopy is corroborated by correlative imaging (Figures 3J and 3K) and Gaussian filtering of dSTORM data (Figures S5D and S5E). Analyzing correlative confocal-dSTORM imaging aimed to clarify the apparent discrepancy between our and previous results. Studies reporting the effect of PHP induction on Brp relied on global thresholding (Weyhersmüller et al., 2011; Goel et al., 2017; Gratz et al., 2019; Böhme et al., 2019); thus, we also used a fixed threshold, which is critical for the results (Figures S5H and S5I).

A molecular concept of homeostatic plasticity

Diverse mechanisms enable the nervous systems to adapt. Among them, PHP stabilizes synapses on timescales of minutes to decades via different pathways (Younger et al., 2013; Orr et al., 2017; Ortega et al., 2018; Frank et al., 2020). Recently, the lysosomal kinesin adaptor Arl8 has been shown to control axonal transport of proteins to presynaptic terminals (Vukoja et al., 2018), and further investigations identified Arl8 to be crucial for material supply during PHP (Goel et al., 2019). However, rapid AZ remodeling seemed to be dispensable for acute but necessary for chronic PHP (Goel et al., 2019; Böhme et al., 2019). As discussed above, our data show no evidence of protein addition to AZs. Thus, the role of Arl8 in PHP needs to be reconsidered. Nevertheless, we cannot rule out the possibility that AZ remodeling during acute and chronic PHP takes place via distinct mechanisms, and future work is needed to dissect these pathways. At *Drosophila* NMJs, a proximodistal gradient in release strength is accompanied by structural adaptations of AZs (Peled and Isacoff, 2011; Ehmann et al., 2014; Paul et al., 2015). Interestingly, we found that PHP increases Brp density regardless of bouton position (Figure S2A).

We describe compaction in Brp clusters and Brp and RBP SCs (Figures 2, 4, and 5E). We focused on quantification of RBP SCs because their dimensions appeared to be particularly interesting

relative to the changes we found for Brp SCs. In principle, it would be interesting to analyze the number of RBP SCs per AZ, but one-channel HDBSCAN analysis did not produce robust results. Two-channel dSTORM using the Brp scaffold as a reference signal might allow quantification of the number of RBP SCs per AZ. Orr et al. (2017) demonstrated that the Semaphorin2b-PlexinB complex regulates PHP via control of presynaptic actin. Although the role of actin in synaptic efficacy has been described unambiguously (Cingolani and Goda, 2008), the significance of AZ compaction remains unclear. Furthermore, other AZ proteins located in membrane proximity, like ENaCs (Younger et al., 2013), presynaptic calcium channels, or RIM, should be examined to determine whether compaction is an even more universal concept during PHP. Finally, it appears promising to correlate transmission properties of individual AZs with their nanoarchitecture using transgenically expressed GCaMP Ca^{2+} sensors to monitor a rise in release probability of initially silent synapses during PHP (Akbergenova et al., 2018; Wentzel et al., 2018; Gratz et al., 2019).

STAR★METHODS

Detailed methods are provided in the online version of this paper and include the following:

- KEY RESOURCES TABLE
- RESOURCE AVAILABILITY
  - Lead contact
  - Materials availability
  - Data and code availability
- EXPERIMENTAL MODEL AND SUBJECT DETAILS
  - Fly stocks
- METHOD DETAILS
  - Philanthotoxin treatment and and larval preparation
  - Fixation, staining and immunofluorescence
  - dSTORM (direct stochastic optical reconstruction microscopy)
  - Confocal microscopy
  - Data evaluation
  - 3D Model of the AZ
- QUANTIFICATION AND STATISTICAL ANALYSIS

SUPPLEMENTAL INFORMATION

Supplemental information can be found online at https://doi.org/10.1016/j.celrep.2021.109770.

ACKNOWLEDGMENTS

This work was supported by the German Research Foundation (DFG) (TRR166/B06 to A.-L.S. and M.H., FOR 3004 SYNABS P1 to M.H., TRR166/B02 to S.D., TRR166/B04 to M.S., and KI1460/5-1 and KI1460/4-1 to R.J.K.) and the IZKF Würzburg (N229 to A.-L.S. and M.H. and Z-3/69 to M.M.P.). The authors thank S. Sigrist for the RBP antibody, T. Langenhan for discussions, and M. Oppmann and F. Köhler for technical assistance.

AUTHOR CONTRIBUTIONS

A.M., J.E., M.S., A.-L.S., M.H., and M.M.P. designed and A.M., M.P., M.H., and M.M.P. performed experiments. A.M., M.P., P.K., F.R., R.J.K., J.E., S.D., M.H., and M.M.P. analyzed data. A.M., M.H., and M.M.P. wrote the manuscript with help from all co-authors. A.-L.S., M.H., and M.M.P. coordinated the study. R.J.K., M.S., A.-L.S., M.H., and M.M.P. provided funding.

DECLARATION OF INTERESTS

The authors declare no competing interests.

Received: November 3, 2020
Revised: May 14, 2021
Accepted: September 7, 2021
Published: October 5, 2021

REFERENCES

Akbergenova, Y., Cunningham, K.L., Zhang, Y.V., Weiss, S., and Littleton, J.T. (2018). Characterization of developmental and molecular factors underlying release heterogeneity at *Drosophila* synapses. eLife *7*, 7.

Altman, D.G., and Bland, J.M. (2011). How to obtain the P value from a confidence interval. BMJ *343*, d2304.

Aponte-Santiago, N.A., and Littleton, J.T. (2020). Synaptic Properties and Plasticity Mechanisms of Invertebrate Tonic and Phasic Neurons. Front. Physiol. *11*, 611982.

Atwood, H.L., and Karunanithi, S. (2002). Diversification of synaptic strength: presynaptic elements. Nat. Rev. Neurosci. *3*, 497–516.

Barg, S., Knowles, M.K., Chen, X., Midorikawa, M., and Almers, W. (2010). Syntaxin clusters assemble reversibly at sites of secretory granules in live cells. Proc. Natl. Acad. Sci. USA *107*, 20804–20809.

Böhme, M.A., Beis, C., Reddy-Alla, S., Reynolds, E., Mampell, M.M., Grasskamp, A.T., Lützkendorf, J., Bergeron, D.D., Driller, J.H., Babikir, H., et al. (2016). Active zone scaffolds differentially accumulate Unc13 isoforms to tune Ca(2+) channel-vesicle coupling. Nat. Neurosci. *19*, 1311–1320.

Böhme, M.A., McCarthy, A.W., Grasskamp, A.T., Beuschel, C.B., Goel, P., Jusyte, M., Laber, D., Huang, S., Rey, U., Petzoldt, A.G., et al. (2019). Rapid active zone remodeling consolidates presynaptic potentiation. Nat. Commun. *10*, 1085.

Campello, R.J., Moulavi, D., and Sander, J. (2013). Density-based clustering based on hierarchical density estimates. In Advances in Knowledge Discovery and Data Mining, J. Pei, V.S. Tseng, L. Cao, H. Motoda, and G. Xu, eds. (Springer), pp. 160–172.

Cheung, P.Y., and Pfeffer, S.R. (2016). Transport vesicle tethering at the trans Golgi network: Coiled coil proteins in action. Front. Cell Dev. Biol. *4*, 18.

Cingolani, L.A., and Goda, Y. (2008). Actin in action: the interplay between the actin cytoskeleton and synaptic efficacy. Nat. Rev. Neurosci. *9*, 344–356.

Davis, G.W., and Goodman, C.S. (1998). Synapse-specific control of synaptic efficacy at the terminals of a single neuron. Nature *392*, 82–86.

Davis, G.W., and Müller, M. (2015). Homeostatic control of presynaptic neurotransmitter release. Annu. Rev. Physiol. *77*, 251–270.

Delvendahl, I., Kita, K., and Müller, M. (2019). Rapid and sustained homeostatic control of presynaptic exocytosis at a central synapse. Proc. Natl. Acad. Sci. USA *116*, 23783–23789.

DiAntonio, A., Petersen, S.A., Heckmann, M., and Goodman, C.S. (1999). Glutamate receptor expression regulates quantal size and quantal content at the Drosophila neuromuscular junction. J. Neurosci. *19*, 3023–3032.

DiCiccio, T.J., and Efron, B. (1996). Bootstrap confidence intervals. Stat. Sci. *11*, 189–228.

Dong, W., Radulovic, T., Goral, R.O., Thomas, C., Suarez Montesinos, M., Guerrero-Given, D., Hagiwara, A., Putzke, T., Hida, Y., Abe, M., et al. (2018). CAST/ELKS Proteins Control Voltage-Gated Ca^{2+} Channel Density and Synaptic Release Probability at a Mammalian Central Synapse. Cell Rep. *24*, 284–293.e6.

Edelsbrunner, H., and Mücke, E.P. (1994). Three-dimensional alpha shapes. ACM Trans. Graph. *13*, 43–72.

Ehmann, N., van de Linde, S., Alon, A., Ljaschenko, D., Keung, X.Z., Holm, T., Rings, A., DiAntonio, A., Hallermann, S., Ashery, U., et al. (2014). Quantitative super-resolution imaging of Bruchpilot distinguishes active zone states. Nat. Commun. *5*, 4650.

Endesfelder, U., Malkusch, S., Fricke, F., and Heilemann, M. (2014). A simple method to estimate the average localization precision of a single-molecule localization microscopy experiment. Histochem. Cell Biol. *141*, 629–638.

Ester, M., Kriegel, H.P., Sander, J., and Xu, X. (1996). A density-based algorithm for discovering clusters in large spatial databases with noise. In Proceedings of the Second International Conference on Advances in Knowledge Discovery and Data Mining, E. Simoudis, J. Han, and U. Fayyad, eds. (AAAI Press), pp. 226–231.

Fouquet, W., Owald, D., Wichmann, C., Mertel, S., Depner, H., Dyba, M., Hallermann, S., Kittel, R.J., Eimer, S., and Sigrist, S.J. (2009). Maturation of active zone assembly by Drosophila Bruchpilot. J. Cell Biol. *186*, 129–145.

Frank, C.A., Kennedy, M.J., Goold, C.P., Marek, K.W., and Davis, G.W. (2006). Mechanisms underlying the rapid induction and sustained expression of synaptic homeostasis. Neuron *52*, 663–677.

Frank, C.A., James, T.D., and Müller, M. (2020). Homeostatic control of Drosophila neuromuscular junction function. Synapse *74*, e22133.

Genç, Ö., and Davis, G.W. (2019). Target-wide Induction and Synapse Type-Specific Robustness of Presynaptic Homeostasis. Curr. Biol. *29*, 3863–3873.e2.

Gillingham, A.K., and Munro, S. (2016). Finding the Golgi: Golgin coiled-coil proteins show the way. Trends Cell Biol. *26*, 399–408.

Goel, P., Li, X., and Dickman, D. (2017). Disparate postsynaptic induction mechanisms ultimately converge to drive the retrograde enhancement of presynaptic efficacy. Cell Rep. *21*, 2339–2347.

Goel, P., Dufour Bergeron, D., Böhme, M.A., Nunnelly, L., Lehmann, M., Buser, C., Walter, A.M., Sigrist, S.J., and Dickman, D. (2019). Homeostatic scaling of active zone scaffolds maintains global synaptic strength. J. Cell Biol. *218*, 1706–1724.

Goodsell, D.S., Olson, A.J., and Forli, S. (2020). Art and Science of the Cellular Mesoscale. Trends Biochem. Sci. *45*, 472–483.

Gratz, S.J., Goel, P., Bruckner, J.J., Hernandez, R.X., Khateeb, K., Macleod, G.T., Dickman, D., and O'Connor-Giles, K.M. (2019). Endogenous Tagging Reveals Differential Regulation of Ca^{2+} Channels at Single Active Zones during Presynaptic Homeostatic Potentiation and Depression. J. Neurosci. *39*, 2416–2429.

Hallermann, S., Kittel, R.J., Wichmann, C., Weyhersmüller, A., Fouquet, W., Mertel, S., Owald, D., Eimer, S., Depner, H., Schwärzel, M., et al. (2010). Naked dense bodies provoke depression. J. Neurosci. *30*, 14340–14345.

Heilemann, M., van de Linde, S., Schüttpelz, M., Kasper, R., Seefeldt, B., Mukherjee, A., Tinnefeld, P., and Sauer, M. (2008). Subdiffraction-resolution fluorescence imaging with conventional fluorescent probes. Angew. Chem. Int.Ed. Engl. *47*, 6172–6176.

Held, R.G., and Kaeser, P.S. (2018). ELKS active zone proteins as multitasking scaffolds for secretion. Open Biol. *8*, 170258.

Held, R.G., Liu, C., and Kaeser, P.S. (2016). ELKS controls the pool of readily releasable vesicles at excitatory synapses through its N-terminal coiled-coil domains. eLife *5*, e14862.

Ho, J., Tumkaya, T., Aryal, S., Choi, H., and Claridge-Chang, A. (2019). Moving beyond P values: data analysis with estimation graphics. Nat. Methods *16*, 565–566.

Hong, H., Zhao, K., Huang, S., Huang, S., Yao, A., Jiang, Y., Sigrist, S., Zhao, L., and Zhang, Y.Q. (2020). Structural Remodeling of Active Zones is associated with synaptic homeostasis. J. Neurosci. *40*, 2817–2827.

Karunanithi, S., Marin, L., Wong, K., and Atwood, H.L. (2002). Quantal size and variation determined by vesicle size in normal and mutant Drosophila glutamatergic synapses. J. Neurosci. *22*, 10267–10276.

Kiskowski, M.A., Hancock, J.F., and Kenworthy, A.K. (2009). On the use of Ripley's K-function and its derivatives to analyze domain size. Biophys. J. *97*, 1095–1103.

Kittel, R.J., and Heckmann, M. (2016). Synaptic vesicle proteins and active zone plasticity. Front. Synaptic Neurosci. *8*, 8.

Kittel, R.J., Wichmann, C., Rasse, T.M., Fouquet, W., Schmidt, M., Schmid, A., Wagh, D.A., Pawlu, C., Kellner, R.R., Willig, K.I., et al. (2006). Bruchpilot promotes active zone assembly, Ca^{2+} channel clustering, and vesicle release. Science *312*, 1051–1054.

Kluyver, T., Ragan-Kelley, B., Pérez, F., Granger, B., Bussonnier, M., Frederic, J., Kelley, K., Hamrick, J., Grout, J., Corlay, S., et al.; Jupyter Development Team (2016). Jupyter Notebooks – a publishing format for reproducible computational workflows. In Positioning and Power in Academic Publishing: Players, Agents and Agendas, F. Loizides and B. Schmidt, eds. (IOS Press), pp. 87–90.

Liu, K.S., Siebert, M., Mertel, S., Knoche, E., Wegener, S., Wichmann, C., Matkovic, T., Muhammad, K., Depner, H., Mettke, C., et al. (2011). RIM-binding protein, a central part of the active zone, is essential for neurotransmitter release. Science *334*, 1565–1569.

Löschberger, A., van de Linde, S., Dabauvalle, M.C., Rieger, B., Heilemann, M., Krohne, G., and Sauer, M. (2012). Super-resolution imaging visualizes the eightfold symmetry of gp210 proteins around the nuclear pore complex and resolves the central channel with nanometer resolution. J. Cell Sci. *125*, 570–575.

Lu, Z., Chouhan, A.K., Borycz, J.A., Lu, Z., Rossano, A.J., Brain, K.L., Zhou, Y., Meinertzhagen, I.A., and Macleod, G.T. (2016). High-Probability Neurotransmitter Release Sites Represent an Energy-Efficient Design. Curr. Biol. *26*, 2562–2571.

Malkusch, S., and Heilemann, M. (2016). Extracting quantitative information from single-molecule super-resolution imaging data with LAMA - LocAlization Microscopy Analyzer. Sci. Rep. *6*, 34486.

McInnes, L., Healy, J., and Astels, S. (2017). hdbscan: Hierarchical density based clustering. J. Open Source Softw. *2*, 205.

Milovanovic, D., Wu, Y., Bian, X., and De Camilli, P. (2018). A liquid phase of synapsin and lipid vesicles. Science *361*, 604–607.

Miskiewicz, K., Jose, L.E., Yeshaw, W.M., Valadas, J.S., Swerts, J., Munck, S., Feiguin, F., Dermaut, B., and Verstreken, P. (2014). HDAC6 is a Bruchpilot deacetylase that facilitates neurotransmitter release. Cell Rep. *8*, 94–102.

Müller, M., Liu, K.S.Y., Sigrist, S.J., and Davis, G.W. (2012). RIM controls homeostatic plasticity through modulation of the readily-releasable vesicle pool. J. Neurosci. *32*, 16574–16585.

Neher, E. (1998). Vesicle pools and Ca^{2+} microdomains: new tools for understanding their roles in neurotransmitter release. Neuron *20*, 389–399.

Neher, E., and Brose, N. (2018). Dynamically primed synaptic vesicle states: Key to understand synaptic short-term plasticity. Neuron *100*, 1283–1291.

Newman, Z.L., Hoagland, A., Aghi, K., Worden, K., Levy, S.L., Son, J.H., Lee, L.P., and Isacoff, E.Y. (2017). Input-Specific Plasticity and Homeostasis at the Drosophila Larval Neuromuscular Junction. Neuron *93*, 1388–1404.e10.

Orr, B.O., Fetter, R.D., and Davis, G.W. (2017). Retrograde semaphorin-plexin signalling drives homeostatic synaptic plasticity. Nature *550*, 109–113.

Ortega, J.M., Genç, Ö., and Davis, G.W. (2018). Molecular mechanisms that stabilize short term synaptic plasticity during presynaptic homeostatic plasticity. eLife *7*, e40385.

Paul, M.M., Pauli, M., Ehmann, N., Hallermann, S., Sauer, M., Kittel, R.J., and Heckmann, M. (2015). Bruchpilot and Synaptotagmin collaborate to drive rapid glutamate release and active zone differentiation. Front. Cell. Neurosci. *9*, 29.

Peled, E.S., and Isacoff, E.Y. (2011). Optical quantal analysis of synaptic transmission in wild-type and rab3-mutant Drosophila motor axons. Nat. Neurosci. *14*, 519–526.

Peled, E.S., Newman, Z.L., and Isacoff, E.Y. (2014). Evoked and spontaneous transmission favored by distinct sets of synapses. Curr. Biol. *24*, 484–493.

Petersen, S.A., Fetter, R.D., Noordermeer, J.N., Goodman, C.S., and DiAntonio, A. (1997). Genetic analysis of glutamate receptors in Drosophila reveals a retrograde signal regulating presynaptic transmitter release. Neuron *19*, 1237–1248.

Robitaille, T.P., Tollerud, E.J., Greenfield, P., Droettboom, M., Bray, E., Aldcroft, T., Davis, M., Ginsburg, A., Price-Whelan, A.M., Kerzendorf, W.E., et al. (2013). Astropy: A community Python package for astronomy. Astron. Astrophys. *558*, A33.

Schindelin, J., Arganda-Carreras, I., Frise, E., Kaynig, V., Longair, M., Pietzsch, T., Preibisch, S., Rueden, C., Saalfeld, S., Schmid, B., et al. (2012). Fiji: an open-source platform for biological-image analysis. Nat. Methods *9*, 676–682.

Schmid, A., Hallermann, S., Kittel, R.J., Khorramshahi, O., Frölich, A.M., Quentin, C., Rasse, T.M., Mertel, S., Heckmann, M., and Sigrist, S.J. (2008). Activity-dependent site-specific changes of glutamate receptor composition in vivo. Nat. Neurosci. *11*, 659–666.

Scholz, N., Ehmann, N., Sachidanandan, D., Imig, C., Cooper, B.H., Jahn, O., Reim, K., Brose, N., Meyer, J., Lamberty, M., et al. (2019). Complexin cooperates with Bruchpilot to tether synaptic vesicles to the active zone cytomatrix. J. Cell Biol. *218*, 1011–1026.

Seabold, S., and Perktold, J. (2010). Statsmodels: Econometric and statistical modeling with python. https://conference.scipy.org/proceedings/scipy2010/seabold.html.

Sieber, J.J., Willig, K.I., Kutzner, C., Gerding-Reimers, C., Harke, B., Donnert, G., Rammner, B., Eggeling, C., Hell, S.W., Grubmüller, H., and Lang, T. (2007). Anatomy and dynamics of a supramolecular membrane protein cluster. Science *317*, 1072–1076.

Stewart, B.A., Atwood, H.L., Renger, J.J., Wang, J., and Wu, C.F. (1994). Improved stability of Drosophila larval neuromuscular preparations in haemolymph-like physiological solutions. J. Comp. Physiol. A Neuroethol. Sens. Neural Behav. Physiol. *175*, 179–191.

Südhof, T.C. (2012). The presynaptic active zone. Neuron *75*, 11–25.

Takamori, S., Holt, M., Stenius, K., Lemke, E.A., Grønborg, M., Riedel, D., Urlaub, H., Schenck, S., Brügger, B., Ringler, P., et al. (2006). Molecular anatomy of a trafficking organelle. Cell *127*, 831–846.

Tang, A.H., Chen, H., Li, T.P., Metzbower, S.R., MacGillavry, H.D., and Blanpied, T.A. (2016). A trans-synaptic nanocolumn aligns neurotransmitter release to receptors. Nature *536*, 210–214.

Tokunaga, M., Imamoto, N., and Sakata-Sogawa, K. (2008). Highly inclined thin illumination enables clear single-molecule imaging in cells. Nat. Methods *5*, 159–161.

van de Linde, S., Sauer, M., and Heilemann, M. (2008). Subdiffraction-resolution fluorescence imaging of proteins in the mitochondrial inner membrane with photoswitchable fluorophores. J. Struct. Biol. *164*, 250–254.

van de Linde, S., Löschberger, A., Klein, T., Heidbreder, M., Wolter, S., Heilemann, M., and Sauer, M. (2011). Direct stochastic optical reconstruction microscopy with standard fluorescent probes. Nat. Protoc. *6*, 991–1009.

van den Bogaart, G., Meyenberg, K., Risselada, H.J., Amin, H., Willig, K.I., Hubrich, B.E., Dier, M., Hell, S.W., Grubmüller, H., Diederichsen, U., and Jahn, R. (2011). Membrane protein sequestering by ionic protein-lipid interactions. Nature *479*, 552–555.

Vukoja, A., Rey, U., Petzoldt, A.G., Ott, C., Vollweiter, D., Quentin, C., Puchkov, D., Reynolds, E., Lehmann, M., Hohensee, S., et al. (2018). Presynaptic Biogenesis Requires Axonal Transport of Lysosome-Related Vesicles. Neuron *99*, 1216–1232.e7.

Wentzel, C., Delvendahl, I., Sydlik, S., Georgiev, O., and Müller, M. (2018). Dysbindin links presynaptic proteasome function to homeostatic recruitment of low release probability vesicles. Nat. Commun. *9*, 267.

Weyhersmüller, A., Hallermann, S., Wagner, N., and Eilers, J. (2011). Rapid active zone remodeling during synaptic plasticity. J. Neurosci. *31*, 6041–6052.

Wolter, S., Schüttpelz, M., Tscherepanow, M., VAN DE Linde, S., Heilemann, M., and Sauer, M. (2010). Real-time computation of subdiffraction-resolution fluorescence images. J. Microsc. *237*, 12–22.

Wolter, S., Löschberger, A., Holm, T., Aufmkolk, S., Dabauvalle, M.C., van de Linde, S., and Sauer, M. (2012). rapidSTORM: accurate, fast open-source software for localization microscopy. Nat. Methods *9*, 1040–1041.

Younger, M.A., Müller, M., Tong, A., Pym, E.C., and Davis, G.W. (2013). A presynaptic ENaC channel drives homeostatic plasticity. Neuron *79*, 1183–1196.

Zhan, H., Bruckner, J., Zhang, Z., and O'Connor-Giles, K. (2016). Three-dimensional imaging of Drosophila motor synapses reveals ultrastructural organizational patterns. J. Neurogenet. *30*, 237–246.

STAR★METHODS

KEY RESOURCES TABLE

REAGENT or RESOURCE	SOURCE	IDENTIFIER
Antibodies		
Normal Goat Serum antibody	Jackson ImmunoResearch Labs	Cat# 005-000-121; RRID:AB_2336990
Mouse monoclonal antibody Brp^{Nc82} anti-Bruchpilot	DSHB	Cat# nc82; RRID:AB_2314866
Rabbit polyclonal antibody anti-RIM-binding protein	Gift from Stephan J. Sigrist; Liu et al., 2011	N/A
F(ab')2-Goat anti-Mouse IgG (H+L) Cross-Adsorbed Secondary Antibody, Alexa Fluor 647	Thermo Fisher Scientific	Cat# A-21237; RRID:AB_2535806
F(ab')2-Goat anti-Rabbit IgG (H+L) Cross-Adsorbed Secondary Antibody, Alexa Fluor 647	Thermo Fisher Scientific	Cat# A-21246; RRID:AB_2535814
Alexa Fluor 488-AffiniPure Goat Anti-Horseradish Peroxidase antibody	Jackson ImmunoResearch Labs	Cat# 123-545-021; RRID:AB_2338965
Chemicals, peptides, and recombinant proteins		
Philanthotoxin 433 tris (trifluoroacetate) salt	Sigma-Aldrich	Cat# P207
Dimethyl sulfoxide (DMSO)	Sigma-Aldrich	Cat# D8418
Triton X-100	Sigma-Aldrich	Cat# T8787
Mercaptoethylamine (MEA)	Sigma-Aldrich	Cat# M6500
Experimental models: Organisms/strains		
Drosophila: wildtype: w^{1118}	BDSC	Flybase ID: FBal0018186
Drosophila: GluRIIA knockout: $DGluRIIA^{AD9}/Df(2L)cl^{h4}$	Gifts from Mathias A. Böhme; Petersen et al., 1997	N/A
Software and algorithms		
rapidSTORM	Wolter et al., 2010, 2012	https://github.com/stevewolter/rapidSTORM
LAMA (LocAlization Microscopy Analyzer)	Malkusch and Heilemann, 2016	RRID:SCR_019133; http://share.smb.uni-frankfurt.de/index.php/software-menue/lama
ZEN Digital Imaging for Light Microscopy (ZEN 12 software, black edition)	Carl Zeiss Microscopy	RRID:SCR_013672; https://www.zeiss.com/microscopy/en_us/products/microscope-software/zen.html
Fiji (v1.440)	Schindelin et al., 2012	RRID:SCR_002285; https://fiji.sc/
Jupyter Notebook	Kluyver et al., 2016	RRID:SCR_018315; https://jupyter.org/
HDBSCAN	McInnes et al., 2017	https://github.com/scikit-learn-contrib/hdbscan
CGAL-Python	INRIA Sophia Antipolis	http://cgal-python.gforge.inria.fr
Astropy	Robitaille et al., 2013	RRID:SCR_018148; https://www.astropy.org/
Statsmodels	Seabold and Perktold, 2010	RRID:SCR_016074; https://www.statsmodels.org/
DABEST	Ho et al., 2019	https://github.com/ACCLAB/DABEST-python
Custom-written Python code	This paper	https://zenodo.org/record/5307692
SigmaPlot 13	Systat Software	RRID:SCR_003210; https://www.sigmaplot.com/products/sigmaplot/
Adobe Illustrator (2015.1.1 release)	Adobe	RRID:SCR_010279; https://www.adobe.com/products/illustrator.html

RESOURCE AVAILABILITY

Lead contact

Further information and requests for resources and reagents should be directed to and will be fulfilled by the lead contact, Mila M. Paul (mila.paul@uni-wuerzburg.de).

Materials availability

This study did not generate new unique reagents.

Data and code availability

All datasets supporting the findings of this work will be shared by the lead contact upon request.

All original code has been deposited at GitHub and is publicly available as of the date of publication. DOIs are listed in the Key resources table.

Any additional information required to reanalyze the data reported in this paper is available from the lead contact upon request.

EXPERIMENTAL MODEL AND SUBJECT DETAILS

Fly stocks

Flies were raised on standard cornmeal and molasses medium at 25°C. *Drosophila melanogaster* male 3rd instar larvae of the following strains were used for experiments: Wild-type: w^{1118} (Bloomington *Drosophila* Stock Center). GluRIIA knockout: $DGluRIIA^{AD9}/Df(2L)cl^{h4}$ (kindly provided by Mathias A. Böhme).

METHOD DETAILS

Philanthotoxin treatment and and larval preparation

Philanthotoxin 433 tris (trifluoroacetate) salt (PhTx, P207 Sigma) was dissolved in dimethyl sulfoxide (DMSO) to obtain a stock solution of 4 mM and stored at −20°C. For each experiment, the respective volume was further diluted with freshly prepared haemolymph-like solution (HL-3; Stewart et al., 1994) to a final PhTx concentration of 20 μM in 0.5% DMSO. Control experiments were performed with the same DMSO concentration in HL-3. PhTx treatment of semi-intact preparations was performed essentially as described previously (Frank et al., 2006). In brief, larvae were pinned down in calcium-free, ice-cold HL-3 at the anterior and posterior endings, followed by a dorsal incision along the longitudinal axis. Larvae were incubated in 10 μl of 20 μM PhTx in DMSO for 10 minutes at room temperature (22°C). Following this incubation time, PhTx was replaced by HL-3 and larval preparations were completed, followed by fixation and staining.

Fixation, staining and immunofluorescence

After PhTx treatment and dissection, larvae were fixed with 4% paraformaldehyde in phosphate buffered saline (PBS) for 10 minutes and blocked for 30 minutes with PBT (PBS containing 0.05% Triton X-100, Sigma) including 5% natural goat serum (Dianova). Primary antibodies were added for overnight staining at 4°C. After two short and three long (20 min each) washing steps with PBT, preparations were incubated with secondary antibodies for 3 hours at room temperature, followed by two short and three long washing steps with PBT. Preparations were kept in PBS at 4°C until imaging. All data were obtained from NMJs formed on abdominal muscles 6/7 in segments A2 and A3, except data for Figure S3, which were obtained from NMJs formed on abdominal muscle 4 in segments A2-A4. Directly compared data (e.g., Figure 2B) were obtained from larvae stained in the same vial and measured in one imaging session.

dSTORM (direct stochastic optical reconstruction microscopy)

Super-resolution imaging of the specimen was performed essentially as previously reported (Ehmann et al., 2014; Paul et al., 2015). Preparations were incubated with monoclonal antibody (mAb) Brp^{Nc82} (1:100, Antibody Registry ID: AB_2314866, Developmental Studies Hybridoma Bank) or a polyclonal antibody against RIM-binding protein (RBP) that maps to a 12 amino acids (aa) peptide near the C-term (aa 1827-1838 of the 1844 aa splice variant; Liu et al., 2011, gift from Stephan Sigrist, 1:1000) and Alexa Fluor647 labeled secondary antibody $F(ab')_2$ fragments goat α-mouse (1:500, A21237, Thermofisher) or α-rabbit (1:1000, A21246, Thermofisher). Boutons were visualized using Alexa Fluor488 conjugated goat α-horseradish-peroxidase antibody (α-hrp, 1:250, Jackson Immuno Research). After staining, larval preparations were incubated in 100 mM mercaptoethylamine (MEA, Sigma-Aldrich) in a 0.2 M sodium phosphate buffer, pH 7.8 to 7.9, to allow reversible switching of single fluorophores during data acquisiton (van de Linde et al., 2008). The buffer additionally included an oxygen-scavenging system (10% (wt/vol) glucose, 10 U/ml glucose oxidase and 200 U/ml catalase). In all experiments, images were acquired using an inverted microscope (Olympus IX-71, 60x, NA 1.49, oil immersion) equipped with a nosepiece-stage (IX2-NPS, Olympus). 647 nm (F-04306-113, MBP Communications Inc.) and 488 nm (iBEAM-SMART-488-S, Toptica) lasers were used for excitation of Alexa Fluor647 and Alexa Fluor488, respectively. Laser beams were passed through clean-up filters (BrightLine HC 642/10, Semrock and ZET 488/10, Chroma, respectively), combined by a

dichroic mirror (LaserMUX BS 473-491R, 1064R, F38-M03, AHF Analysentechnik), and directed onto the probe by an excitation dichroic mirror (HC Quadband BS R405/488/532/635, F73-832, AHF Analysentechnik). The emitted fluorescence was filtered with a quadband-filter (HC-quadband 446/523/600/677, Semrock) and a longpass- (Edge Basic 635, Semrock) or bandpass-filter (Brightline HC 582/75, Semrock) for the red and green channel, respectively, and divided onto two cameras (iXon Ultra DU-897-U, Andor) using a dichroic mirror (HC-BS 640 imaging, Semrock). The green channel was used for visualizing individual presynaptic boutons in normal fluorescence microscopy. For the red channel, image resolution was 126 nm x 126 nm or 127 nm x 127 nm per pixel to obtain super-resolution of Brp. Single fluorophores were localized and high resolution-images were reconstructed with rapidSTORM (Heilemann et al., 2008; van de Linde et al., 2011; Wolter et al., 2010, 2012; https://www.biozentrum.uni-wuerzburg.de/super-resolution/). Only fluorescence spots with more than 12 000 photons were analyzed. Localization precision was determined with the NeNa algorithm (nearest neighbor based analysis; Endesfelder et al., 2014), implemented in the LAMA software package (LocAlization Microscopy Analyzer; Malkusch and Heilemann, 2016) in 108 dSTORM measurements of Brp and was 6.3 ± 0.6 nm (mean ± SD) in this study.

Confocal microscopy

For confocal imaging larvae were mounted in PBS and imaged using a commercial confocal laser scanning microscope (Zeiss LSM 700) equipped with an oil-immersion objective (Plan-Apochromat 63x/1.40 Oil M27). Alexa Fluor647 and Alexa Fluor488 were excited with the 639 nm and the 488 nm diodes, respectively. The microscope was controlled via ZEN 12 software (black edition, Zeiss AG). For each z stack 5-13 slices with 200 nm axial spacing were obtained. The gain of the photomultiplier tubes was adjusted to 700 and 600 V and laser power was set to 1.5% and 1% in the red and green channel, respectively, to obtain a good signal with little photobleaching allowing subsequent dSTORM imaging. The pinhole was set to 70.6 μm, corresponding to 1.32 Airy units in the red and 1.73 Airy units in the green channel. Images were recorded in 1024 × 1024 (lines x pixels) format with 16-bit data depth. Given an approximate resolution of 200 nm in the red channel, the pixel size, adjusting the zoom factor to 1.2, was set to about 83 nm for sufficient data sampling. Settings resulted in a pixel dwell time of 3.15 μs.

Data evaluation

Cluster analysis

Localization microscopy data were analyzed with custom written Python code (https://www.python.org/; language version 3.6) and the web-based Python interface Jupyter (https://jupyter.org/index.html). Localization tables from rapidSTORM were directly loaded and analyzed. Prior to the Python-based analysis the regions of interest (ROI) were masked in the reconstructed, 10 nm px^{-1} binned images from rapidSTORM using FIJI (1.440; Schindelin et al., 2012). These ROIs corresponded to the terminal 6 boutons according to the α-hrp staining. In earlier work on super-resolved Brp-data, density-based spatial clustering of applications with noise (DBSCAN) was used to identify active zone (AZ) subclusters (SCs; Ehmann et al., 2014). Given the parameters k and ε, DBSCAN considers a group of localizations as a cluster if there are at least k residues in a circle with radius ε around a certain localization (Ester et al., 1996). Here, we used an improved approach called hierarchical density-based spatial clustering of applications with noise (HDBSCAN) that, in contrast, extracts the most robust clusters from a cluster hierarchy over varying ε environments that are least sensible to ε variation, i.e., have the longest lifetime in the cluster tree (Campello et al., 2013). The algorithm is thus more powerful for cluster detection in data with variable density. We used the Python implementation of HDBSCAN (McInnes et al., 2017; https://github.com/scikit-learn-contrib/hdbscan), which takes 'minimum cluster size' and 'minimum samples' as the main free parameters, and performed two steps of clustering with different parameters on our Brp localization data: (i) to identify the AZs, and (ii) to extract the SCs from the AZs. Setting minimum samples to smaller values than minimum cluster size allows the algorithm to be less conservative, i.e., extract clusters that might be smaller than minimum cluster size but very robust in the cluster hierarchy. We explored optimal clustering parameters for the detection of AZs and varied minimum cluster size and minimum samples in a certain range (Figure 1B; Figure S1). Too high values falsely merge adjacent AZs together (Figure 1C) whereas too low values lead to fragmenting AZs into smaller clusters (Figure 1E). A wide range of parameters delivered robust results and all Brp clusters in this study were extracted with the combination 100 and 25 for minimum cluster size and minimum samples. A second HDBSCAN on the individual AZ clusters was performed with minimum cluster size 24 and minimum samples 6, and a similar number of SCs with a comparable spatial extent compared to the DBSCAN-based SC analysis of Ehmann et al., 2014 was found (compare Figure 1H for SC radii and Figures 2F and 2H for SC areas). For SC analysis, the cluster selection method was changed to 'leaf' clustering, which comprises a tendency to more homogeneous clusters by extracting those that lie on leaf nodes of the cluster tree rather than the most stable clusters. For analysis of RBP localization data two levels of HDBSCAN clustering were carried out to identify large RBP clusters in the first step (not shown) and to extract the SCs from these large clusters in the second step (Figure 4B, minimum cluster size and minimum samples were adjusted to 8 and 2, respectively). To quantify cluster area, we computed 2D alpha shapes using CGAL (Computational Geometry Algorithms Library; https://www.cgal.org) in Python. The geometrical concept of alpha shapes can be used to calculate the shape and thus the area of a set of points. Given a finite set of points and an alpha value α, an edge of the shape is drawn between two points whenever they lie on the boundary of a disk with radius $\alpha^{1/2}$ that does not contain any other point (Edelsbrunner and Mücke, 1994). To get the alpha shapes of the AZ clusters and AZ SCs we choose α-values of 800 nm^2 and 300 nm^2, respectively. The SC center of mass (c.o.m.) was calculated as mean of the x- and y-values of all localizations of the SC, and the AZ c.o.m. as mean of its SC c.o.m.s. To estimate the distance of SC c.o.m. from AZ c.o.m. the Euclidean distance of these points

was computed. The distance to the nearest SC c.o.m. was determined for each individual SC c.o.m. and the mean value per AZ was obtained (Figures S2H and S2I). To get the distance between SCs the mean SC radius per AZ was subtracted from the SC center distance (Figures S2J and S2K). For evaluation of Brp cluster circularity, the ratio of the Eigenvalues of each cluster was computed, where 1 indicates a perfect circle and values < 1 indicate decreasing circularity (Figure S2C). Exclusion criteria for outliers in all dSTORM data evaluations of Brp were AZ area $\leq$ 0.03 μm^2 (Ehmann et al., 2014) and $\geq$ 0.3 μm^2, absolute localization counts per AZ $\geq$ 8000 and mean AZ localization density $\geq$ 60000 localizations per μm^2 (about 3-5-fold median). Additional exclusion criteria for type Ib neuron recordings of Brp were average AZ localization count < 1000 and at the same time average AZ area < 0.095 μm^2 per image, indicative of insufficient data quality, as well as a mean A/D count per AZ $\leq$ 45000 if the mean A/D count of all AZs in one or more experimental groups was < 50000, indicative of weaker illumination. Exclusion criteria for first level RBP clusters were area $\leq$ 0.01 μm^2 and $\geq$ 0.1 μm^2, absolute localization counts per cluster $\geq$ 1500 and mean localization density $\geq$ 40000 localizations per μm^2. The H function (Figures 1F and 4C) as derivative of Ripley's K function was computed using Python package Astropy (Robitaille et al., 2013) for each individual AZ (respectively first level RBP cluster) and for a random Poisson distribution. Curves for display were averaged (mean ± SD). The function was evaluated in nm steps for radii from 0 to 120 nm and without correction for edge effects.

Localization data visualization

For visualization of the localization-based results in Figures 1A, 1C–1E, 1G, 2A, 2C, 2E, 2G, 3C, 4A, 4B, S2E, and S3A scatterplots were created in Python. For visualization of representative dSTORM measurements in Figures 3B, 3H, 3I, S5A, S5B, and S5F, reconstructed images from rapidSTORM with 5 nm binning were opened in FIJI and were contrast enhanced for clarity where necessary.

Simulation of localization clusters

Simulated localization data (Figure S4) for a given radius r were created in Python using the function numpy.random.uniform() passing the arguments -r and r. Thus, random numbers > = -r and < r were created and used as x- and y-coordinates of random points. Simulation was further constrained by computing the Euclidean distance of the simulated point and the center of the simulated point cloud (x = 0, y = 0) and discarding all points with a distance > r. This gave rise to point clouds consisting of 1500 points with circular distributions in a circle with radius r around the center. For HDBSCAN analysis nine random point clouds per given radius in the same coordinate system were used as input spacing the center points of adjacent point clouds three radii apart. To 'simulate' confocal resolution the point coordinates were binned into 5 nm pixels. Binned images were imported as text images in FIJI and automatically converted to 32-bit images where raw integrated density is equal to the absolute number of localizations in a pixel. A Gaussian filter with 150 nm standard deviation (SD) was applied to blur the images. The maximally possible pixel intensity after blurring was 0.265 arbitrary units (a. u.) corresponding to 1500 points in one pixel before blurring. To achieve a somewhat realistic gain all images were equally scaled to a maximum of 0.35 a. u. Thresholding was performed in 8-bit with 50 a. u.

Analysis of confocal data

Confocal images were processed and evaluated in FIJI. Z stacks were maximum projected and Brp spots segmented with a pixel intensity threshold of 100 a. u. in 8-bit using the 'Analyze Particles' function (see Figure 3Aii). Mean pixel intensity of resulting masks was measured in the original images. The following procedure was used for correlative analyses presented in Figures 3D–3G. Corresponding Brp spots, extracted with 100 a. u. threshold, and Brp localization clusters were assigned manually. Only clusters that were clearly distinguishable in both confocal and dSTORM without confluence to neighboring signal were used. Bouton height ranged from 0.8 to 2 μm in confocal imaging. To ensure comparability to earlier quantification approaches we created maximum projections of confocal data. The capture range of our dSTORM measurements is at least 1 μm, but probably even higher (Tokunaga et al., 2008). To minimize bias arising from analysis of different focal planes we inspected all correlative images and found no evidence for signal that was included in confocal stacks but missing in dSTORM images (compare Figures 3Ai and 3B). Additionally, only AZs were correlated that could be clearly assigned in both imaging techniques. Localization data from sequential imaging shown in Figures 3J and 3K were analyzed as described above. For confocal analysis, here, only pixels in the same ROIs used for the localization-based analysis were included. Data for correlative analysis (Figures 3J and 3K) were extracted with 100 a. u. in 8-bit and were additionally analyzed with further intensity thresholds (Figures S5H and S5I).

Gaussian filtering of dSTORM data

To obtain confocal resolution from our dSTORM data (Figures S5A and S5B) localization tables from rapidSTORM with 5 nm binning were converted to FIJI-readable density matrices where raw integrated density corresponds to the localization count in a pixel. Images were contrast enhanced to obtain 0.1% saturated pixels, a Gaussian filter with 150 nm SD was applied and the images were scaled to a pixel size of 80 nm. The same images as for the localization-based analysis were included and only pixels in the same ROIs as described above were used for subsequent processing and analysis. Images were converted to 8-bit and the gain was adjusted by scaling all pixels in both images to the same value by setting the brightest of all analyzed pixels in all images to the maximum value of 255 a. u.. Following a standard protocol for the quantification of confocal data of the *Drosophila* NMJ (Schmid et al., 2008; Weyhersmüller et al., 2011) a minimal threshold of 50 a. u. was applied, and the 'Analyze Particles' function in FIJI was used to create individual masks from the thresholded images. The resulting masks were applied to the non-thresholded Gaussian filtered images to quantify AZ area as well as the mean intensity of AZs. STED resolution in Figure S5F was obtained similarly, but a Gaussian filter with 25 nm SD was applied to the density matrices. The gain of all images was adjusted by setting 175 a. u. to the maximum. AZ area and mean pixel intensity per AZ were measured with a threshold of 50 a. u. (Weyhersmüller et al., 2011) and only Brp spots with an area > 0.03 μm^2 were analyzed. The diameter of Brp spots was calculated under the assumption of a circular area ($d = 2^* \sqrt{(A/\pi)}$; d: Brp spot diameter, A: Brp spot area). To quantify intensity maxima per AZ planar-oriented, ring-like

AZs were selected. Selection was performed blinded with respect to the experimental groups. AZs were cut out from images. Thresholding was performed with 100 a. u. and all pixels below the threshold were removed. The maxima were extracted using the 'Find Maxima' function in FIJI (Prominence = 0) and quantified per AZ.

3D Model of the AZ

We generated a 3D model of the *Drosophila* presynaptic AZ (Figure 5E; Video S1) using Blender 2.92.0 (https://www.blender.org). This model includes spheres representing synaptic vesicles with a diameter of 40 nm plus a protein coat of 10 nm in each direction and spheres representing RBP SCs with diameters of 27.4 nm for ctrl (n = 10) and 25.4 nm for GluRIIAko (n = 10). The radial distance of RBP SCs was approximately 97 nm for both ctrl and GluRIIAko. In addition, the model contains a Brp dome with a diameter of 369.2 nm for ctrl and 349.6 nm for GluRIIAko with 15 smaller domes on its surface representing Brp SCs with a diameter of 45 nm for ctrl and 43.4 nm for GluRIIAko. The radial distance of Brp SCs was approximately 116 nm for ctrl and 113 nm for GluRIIAko. All diameters given above were calculated from the values shown in Table S1A taking the square root from the protein area divided by π.

QUANTIFICATION AND STATISTICAL ANALYSIS

Statistical analyses were performed with Sigma Plot 13 (Systat Software) or Python 3.9 using statsmodels 0.12.2 (Seabold and Perktold, 2010). Shapiro-Wilk was used to test normality. If data were not normally distributed, we used the non-parametric Mann-Whitney rank sum test for statistical analysis and reported data as median (25^{th}-75^{th} percentile). If data were normally distributed they were reported as mean ± SD unless indicated otherwise (Figure 1F) and two-tailed t test was performed to evaluate statistical significance (Table S1C). Asterisks indicate the significance level (* $p < 0.05$, ** $p < 0.01$, *** $p < 0.001$) and n denotes sample number. In boxplots, horizontal lines represent median, boxes quartiles and whiskers 10^{th} and 90^{th} percentiles. Scatterplots show individual data points unless indicated otherwise. Bin counts in histograms were normalized to the total number of observed events which was set to 1. Color codes in contour plots (Figure 1B; Figure S1) were logarithmically scaled. Linear regression curves were fitted and Spearman correlation coefficient r and statistical significance p of correlations were evaluated in Sigma Plot. All plots were produced with Sigma Plot except plots for Figure S7 which was created with Matplotlib, and plots for Figure S6 which were created with Python modulde DABEST (Ho et al., 2019). Figures were assembled using Adobe Illustrator (Adobe, 2015.1.1 release). Tables S1A–S1D contain all numerical values not stated in text and figure legends including p values and samples sizes. Several replicates of dSTORM experiments were carried out to assure robustness of the observed effects.